Energy Storage Materials 87 (2026) 105045

Contents lists available at ScienceDirect

Energy Storage Materials

journal homepage: www.elsevier.com/locate/ensm

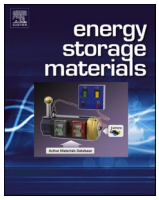

Compromise between energy density and stability: Proper capacity balancing enables high-performance solid-state batteries

Ruizhuo Zhang [a], Seyedhosein Payandeh [a], Yuan Ma [a], Damian Goonetilleke [a], Yushu Tang [b], Aleksandr Kondrakov [a,c,**], Jürgen Janek [a,d], Torsten Brezesinski [a,*]

[a] Battery and Electrochemistry Laboratory (BELLA), Institute of Nanotechnology, Karlsruhe Institute of Technology (KIT), Kaiserstr. 12, 76131 Karlsruhe, Germany
[b] Institute of Nanotechnology, Karlsruhe Institute of Technology (KIT), Kaiserstr. 12, 76131 Karlsruhe, Germany
[c] BASF SE, Carl-Bosch-Str. 38, 67056 Ludwigshafen, Germany
[d] Institute of Physical Chemistry & Center for Materials Research (ZfM/LaMa), Justus-Liebig-University Giessen, Heinrich-Buff-Ring 17, 35392 Giessen, Germany

ARTICLE INFO

Keywords:
All-solid-state battery
Slurry casting
Ni-rich cathode
Thiophosphate solid electrolyte
Three-electrode cells

ABSTRACT

Controlling electro-chemo-mechanical effects remains a key challenge in advancing the development of solid-state batteries (SSBs) with layered Ni-rich cathode and sulfide solid electrolyte. While surface coatings suppress parasitic side reactions, mechanical failure can still be severe, and there is a relative lack of effective strategies to counteract it. To improve the integrity of the cathode, herein we propose a capacity balancing approach with $Li_4Ti_5O_{12}$ (LTO) as a model anode in thiophosphate-based SSBs. By leveraging the tip-shaped lithiation tail of LTO with a low negative-to-positive balancing (LB), this strategy enables a reduced upper cut-off potential of the $LiNi_{0.85}Co_{0.10}Mn_{0.05}O_2$ (NCM85) cathode used, thereby mitigating mechanical stress/strain induced by the H2-H3 phase transition. As polarization increases during cycling, the potential is gradually increased, compensating for the loss of capacity without external voltage adjustment. Three-electrode measurements validate the proposed mechanism across several C-rates and corroborate this self-regulating process. Unlike high negative-to-positive balancing (HB), the LB configuration achieves improved structural integrity, reduced charge-transfer resistance, and prolonged cycle life, retaining 80 % capacity after about 1300 cycles at 1C (compared to 400 cycles in HB cells). Overall, this work offers a simple, yet effective strategy for extending the longevity of cathodes for the development of high-performance SSBs.

1. Introduction

Solid-state batteries (SSBs) have been established as a next-generation electrochemical energy storage technology, promising higher energy densities and safety compared to conventional lithium-ion batteries (LIBs) [1,2]. Replacing the flammable liquid electrolyte in LIBs with a superionic solid electrolyte (SE) eliminates the risk of leakage and combustion while also making the use of lithium metal anodes for further energy density improvements feasible. Among the different classes of SEs, sulfides (thiophosphates) stand out due to their superior room-temperature ionic conductivity (up to 10^{-2} S cm^{-1}) and favorable mechanical softness, ultimately enabling close contact with the other (active/inactive) electrode components [3–5]. In parallel, the development of layered Ni-rich oxide cathode active materials (CAMs), such as polycrystalline $LiNi_{0.85}Co_{0.10}Mn_{0.05}O_2$ (NCM85) or even single crystal counterparts, offers high energy density and renders them attractive candidates for coupling with sulfide SEs in SSBs [6–8].

In general, the combination of Ni-rich cathodes and sulfide SEs is a promising route toward realizing high-performance (practical) SSBs. However, this configuration presents substantial challenges, particularly at the interface between CAM and SE [9–11]. Electrochemical side reactions can lead to the formation of resistive interphases and microstructural degradation of the CAM particles. To address this, protective coatings, such as $LiNbO_3$, have been widely employed for passivating the cathode surface and suppress the decomposition of SE [6,12–14]. While coating strategies have generally proven effective in improving (electro) chemical stability, particularly in terms of increasing initial capacity and reversibility, mechanical degradation, including intergranular particle cracking and/or contact loss, remains a major obstacle to the longevity of SSBs [14–17].

* Corresponding author.
** Corresponding author at: BASF SE, Carl-Bosch-Str. 38, 67056 Ludwigshafen, Germany.
E-mail addresses: aleksandr.kondrakov@basf.com (A. Kondrakov), torsten.brezesinski@kit.edu (T. Brezesinski).

https://doi.org/10.1016/j.ensm.2026.105045
Received 12 January 2026; Received in revised form 6 March 2026; Accepted 14 March 2026
Available online 15 March 2026

To mitigate adverse mechanical effects, the optimization of components within the cathode, for example, using glassy SEs and/or tailored polymer binders, has been intensively investigated [18–21]. It should be noted that, in the preparation of scalable cathodes, binder-containing electrodes are usually produced either by slurry casting (wet processing) or by dry processing [18,22,23]. Compared with (rigid) pelletized electrodes, slurry-cast tapes not only improve mechanical cohesion within the electrode, but also help accommodate volume variations of the CAM, thereby increasing stability and enhancing cyclability.

Despite these advances, it is the CAM itself that plays a decisive role in determining the performance and energy density of SSBs. Consequently, a fundamental trade-off exists between maximizing the specific capacity of Ni-rich cathodes and ensuring long-term stability, which is regulated by their proper use. While operation at a high upper cut-off potential (UP) enables better utilization of the lithium inventory, it inevitably exacerbates structural degradation arising from intrinsic phase transitions. Lowering the UP mitigates mechanical stress/strain and improves interfacial stability, but this benefit is accompanied by a sacrifice in capacity. In addition, prolonged operation leads to electrochemical degradation, as interphases continuously grow and microstructural damage occurs, eventually resulting in cell polarization and capacity fading.

To overcome this, in the present work, we propose an adaptive compensation strategy through the rational design of capacity balancing. Using polycrystalline NCM85 coated with amorphous $LiNbO_3$ ($LiNbO_3$-NCM85) and processed into slurry-cast electrodes, we paired the cathode (working electrode, WE) with carbon-coated $Li_4Ti_5O_{12}$ (LTO) as a model anode (counter electrode, CE). Under low balancing (LB) conditions with a negative-to-positive (n/p) capacity ratio of 1.1, the tip-shaped lithiation tail of LTO is used to lower the initial upper cut-off potential (IUP) of the WE, thereby mitigating the H2-H3-induced volume change and associated mechanical degradation of the Ni-rich cathode. Over the course of cycling, electro-chemo-mechanical degradation gradually leads to polarization, which ultimately increases the UP to the desired UP (DUP) and helps compensate for the loss of capacity without requiring active control of the voltage window. This LB design greatly improves cycling stability by increasing the mechanical integrity of the cathode.

Taken together, our findings establish capacity balancing as a powerful strategy to reconcile high energy output and long-term cycling stability in sulfide-based SSBs with a Ni-rich cathode. In particular, the LB approach offers new design/mechanistic perspectives under realistic manufacturing conditions.

2. Results and discussion

To improve the (electro)chemical stability at the interface between CAM and SE, $LiNbO_3$ was applied to the surface of the NCM85 particles using a sol-gel process [13]. Powder X-ray diffraction (XRD) patterns of both pristine NCM85 and $LiNbO_3$-NCM85 are presented in Figure S1. As can be seen, the reflections before and after coating matched, indicating a well-preserved layered structure ($R\bar{3}m$ space group) without new peaks due to the low content (1 wt. %) and amorphous nature of $LiNbO_3$. Scanning electron microscopy coupled with energy dispersive X-ray spectroscopy (SEM-EDS) revealed that $LiNbO_3$ forms a continuous shell around the secondary particles (see Figure S2a–g) without noticeable inhomogeneities. The average size of the $LiNbO_3$-NCM85 particles was about 4 μm, and they had a nearly spherical shape. The as-made $LiNbO_3$-NCM85 and argyrodite Li_6PS_5Cl (LPSCl) were then used as main components for the assembly and testing of SSBs.

2.1. Cathode microstructure and ionic/electronic partial conductivities

As a well-recognized approach for improving the mechanical stability of electrodes, a binder-containing cathode was produced by wet processing for electrochemical testing. To investigate the effects of the added polymer binder and the slurry casting process on the cathode in terms of effective ionic/electronic partial conductivities and microstructure, a pelletized cathode was also produced and measured in parallel. Ball milling was used to produce the cathode composite by dry mixing $LiNbO_3$-NCM85 CAM, LPSCl SE, and Super C65 carbon additive, as shown in Fig. 1a. The composite obtained can be compacted directly and used as a cathode in SSBs, which is often implemented in laboratory-scale research. To produce the slurry-cast cathode, a polyisobutylene (PIB) binder and *o*-xylene as nonpolar solvent were added to the aforementioned composite (see Fig. 1e), after which the mixture was coated onto Al foil. Further details can be found in the Experimental section.

A cathode with a smooth surface was achieved using 1 wt. % binder (see Fig. 1f). In the pristine state (without compaction), the morphology of the CAM and SE particles and their distribution were first examined through top-view SEM-EDS imaging. As is evident from Fig. 1b, agglomerated SE particles were closely surrounded by the CAM. To evaluate the microstructure after densification, both the pelletized and slurry-cast cathodes were subject to compaction at 435 MPa. As shown in Fig. 1c and d, the slurry-cast cathode was much denser than its pelletized counterpart, due to better elimination of macroscopic pores/voids. Interestingly, most of the pores/voids in the pelletized cathode were concentrated in areas where the CAM tends to agglomerate, creating relatively large gaps between the rigid CAM "clusters" and the deformable SE particles. In contrast, the improved dispersion of particles achieved by slurry casting ensures a more uniform embedding of the CAM. Specifically, the insulating PIB binder, which appears to be evenly distributed across the cathode, formed an adhesive film that holds the composite together and reduces porosity. After compaction, the "island-like" SE domains observed in the pelletized cathode were clearly smaller and better distributed, resulting in improved ionic percolation through the slurry-cast cathode.

To quantify how the microstructural differences affect the charge-transport properties, ion- and electron-blocking cell configurations were used, as shown in Figure S3a and b. To mimic the conditions of the actual SSBs, the same assembling/operating pressures and temperature were used for AC polarization measurements. The effective ionic/electronic partial conductivities were eventually extracted by fitting impedance data using specific transmission line models (see Figure S3c–f). As shown in Fig. 1g and Table S1, the pelletized cathode exhibited an ionic conductivity (σ_{ion}) that was about 2.6 times higher than that of the slurry-cast cathode (0.37 versus 0.14 mS cm^{-1}). A similar observation was made for the electronic conductivity (σ_{el}), but to a much greater extent ($1.3\bullet10^{-1}$ versus $4.8\bullet10^{-2}$ mS cm^{-1}). It should be noted that, in addition to the volume ratio of CAM to SE and the carbon content, the nature/properties of the selected binder also strongly determine the percolation paths for ion and electron transport. Regardless, the binder impairs charge transport, at least to some degree, especially when it is finely distributed in the cathode. Nevertheless, the slurry-cast cathode preserved relatively high ionic and electronic partial conductivities while offering greater mechanical stability than the pelletized counterpart, which is required for stable SSB operation.

2.2. Capacity balancing and cell cyclability

As mentioned above, LTO was employed as a model anode in the present work. To determine the specific capacity that can be achieved with the individual electrodes, SSBs were assembled with indium-lithium alloy (In/InLi) as CE (0.62 V vs. Li^+/Li). The In/InLi|LPSCl|LTO and In/InLi|LPSCl|$LiNbO_3$-NCM85 cells were cycled between 0.38 and 1.38 V vs. In/InLi (equivalent to approx. 1.0–2.0 V vs. Li^+/Li) and between 2.28 and 3.68 V vs. In/InLi (equivalent to approx. 2.9–4.3 V vs. Li^+/Li), respectively. Cells of configuration LTO|LPSCl|NCM85 were also operated within a 1.4 V window, namely from 1.35 to 2.75 V vs. $Li_4Ti_5O_{12}/Li_7Ti_5O_{12}$. All electrochemical measurements were performed at 45 °C and under a constant external pressure of 81 MPa. As shown in

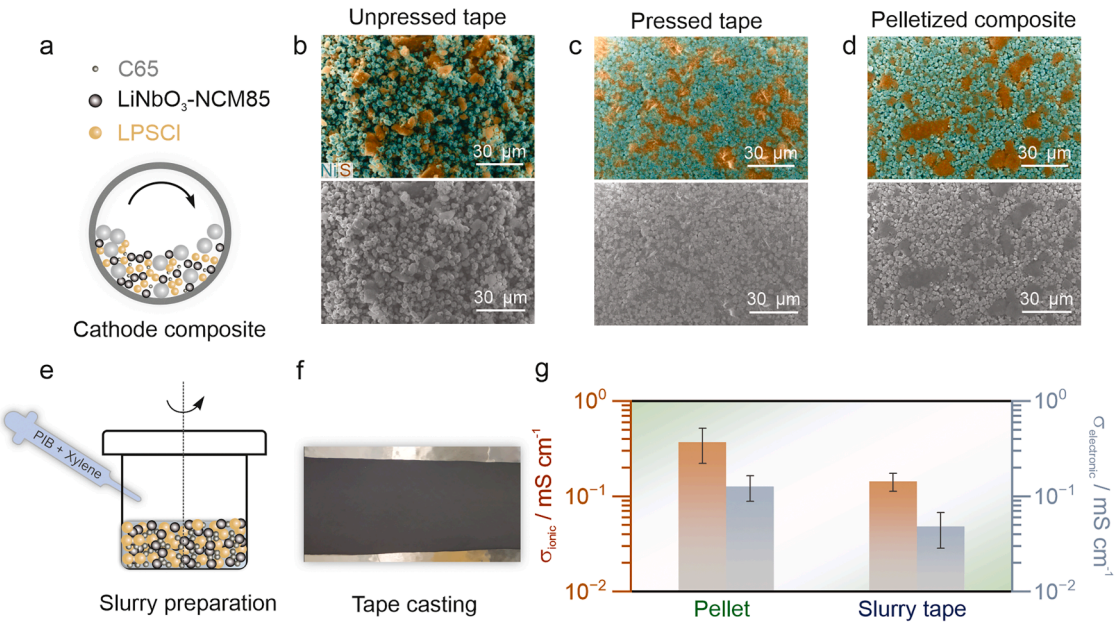

Fig. 1. Microstructure and transport properties of slurry-cast and pelletized cathodes. Schematic representation (a) of the dry mixing of cathode composite by ball milling and (e) of the subsequent slurry preparation with PIB binder and *o*-xylene as solvent. Top-view SEM images in conjunction with EDS mapping of nickel and sulfur for the slurry-cast cathode (b) before and (c) after compaction at 435 MPa, as well as (d) for the pelletized cathode. (f) Photograph of the slurry-cast cathode. (g) Effective ionic and electronic partial conductivities from three independent cells determined by AC polarization at 81 MPa and 45 °C.

Figure S4a, the In/InLi-based cells underwent two formation cycles at 0.1C, followed by two cycles at 0.2C. The $LiNbO_3$-NCM85 cathode exhibited an initial Coulomb efficiency of 90.4 %, indicating good interfacial stability due to the presence of a protective $LiNbO_3$ coating. LTO, known for its high mechanical robustness and compatibility with sulfide SEs, is widely used in SSB systems as a zero-strain anode. As shown in Figure S5, the material employed retained about 97 % of its initial capacity after 200 cycles at 0.2C (~131 mAh g_{LTO}^{-1}), suggesting negligible capacity fading from LTO. From the fourth-cycle lithiation/delithiation profiles in Figure S4b and c, it can be seen that both $LiNbO_3$-NCM85 and LTO exhibit high reversibility (Coulomb efficiency).

When LTO is used as an anode (CE) in the electrochemical testing of SSBs, a relatively high n/p capacity ratio is typically sought to maintain the plateau at 1.55 V vs. Li^+/Li as a reliable reference potential. Notably, the discharge profile showed a gradual potential drop upon approaching the cut-off potential during lithiation (see Figure S4c), where LTO transitions from a two-phase coexistence region to the rock-salt $Li_7Ti_5O_{12}$ phase. As can be seen, this tip-shaped lithiation tail contributes significant capacity at low potentials. Therefore, using the fourth-cycle specific capacities, q_{ch} = 202 mAh g^{-1} for $LiNbO_3$-NCM85 and q_{dis} = 132 mAh g^{-1} for LTO, we focused on two capacity balancing conditions, namely high balancing (HB, n/p = 1.5) and low balancing (LB, n/p = 1.1), as shown in Fig. 2a. The core difference lies in the way the LTO lithiation profile is used. In HB cells, the LTO anode operates entirely within the voltage plateau region, whereas in LB cells, due to the constrained voltage window, the potential of the LTO anode falls below the plateau toward the end of the charging process. This leads to a lower upper cut-off potential (UP, ~4.2 V vs. Li^+/Li) for the $LiNbO_3$-NCM85 cathode in the LB cells. As a result, the LB design deliberately reduces the initial upper cut-off potential (IUP) at the expense of some capacity to mitigate the H2-H3 phase transition that typically occurs above 4.2 V vs. Li^+/Li in Ni-rich cathodes (thereby indirectly affecting mechanical integrity). For practical implementation, the capacity balancing was controlled by tailoring the mass of the LTO composite (see Experimental section).

The first-cycle voltage profiles of the HB and LB cells at 0.2C in Fig. 2b confirm the expected differences in achievable specific charge/discharge capacities with 227/198 mAh g_{NCM85}^{-1} and 210/185 mAh g_{NCM85}^{-1}, respectively. With the same charge capacity as in the LB case, the cut-off voltage of the HB cell would be about 2.65 V vs. $Li_4Ti_5O_{12}$/$Li_7Ti_5O_{12}$ (corresponding to ~4.2 V vs. Li^+/Li), which is consistent with the reduction in IUP in the LB cells.

Differential capacity (dq/dV) curves of the initial cycle (see Figure S6a) show clear H1-M-H2-H3 phase transitions for both configurations. However, the H2-H3 peak is significantly weaker in the LB cells. Since this high-voltage transition causes large volume changes and irreversible structural damage to Ni-rich cathodes, the LB condition apparently helps reduce the formation of mechanical stresses and thus improves stability.

As shown in Fig. 2c and d, the HB and LB cells exhibit distinct differences in capacity retention at 0.2C. Considering the cell-to-cell variations frequently observed in the testing of SSBs and the need for repeated measurements and statistical averaging for an objective evaluation of the proposed strategies, the long-term cycle data presented here represent the average of two independent cells [24]. The HB configuration started with a higher initial specific discharge capacity of q_{dis} = 199 mAh g_{NCM85}^{-1}, but retained only ~85 % (169 mAh g_{NCM85}^{-1}) after 120 cycles. In contrast, despite a lower starting value of q_{dis} = 185 mAh g_{NCM85}^{-1}, the LB configuration achieved a higher capacity retention of ~94 %, corresponding to 173 mAh g_{NCM85}^{-1}, demonstrating the beneficial effect of the capacity balancing strategy. Regardless, both exhibited average Coulomb efficiencies of φ = 99.6 % (HB) and 99.8 % (LB), confirming the high reversibility. The superior capacity retention of the LB cells is based on two synergistic effects: (i) improved structural integrity of the cathode due to a lower IUP and (ii) gradual increase in UP during cycling, which adaptively compensates for polarization-related capacity fading.

Evidence of the latter can be found in the 2D and 3D contour plots of the differential capacity for the charging process in Fig. 2e and f and Figure S7a and b, respectively. Focusing on the evolution of the H2-H3 transition (~2.65 V vs. $Li_4Ti_5O_{12}$/$Li_7Ti_5O_{12}$), the peak intensity in the HB cells clearly decreased with cycling, indicating a loss of reversible capacity in this potential range, likely due to structural degradation of the CAM. By contrast, in the LB case, the peak intensity increased, pointing toward a gradual rise in UP that counteracts the capacity decay caused by degradation. After 120 cycles (see Figure S6b), the peaks

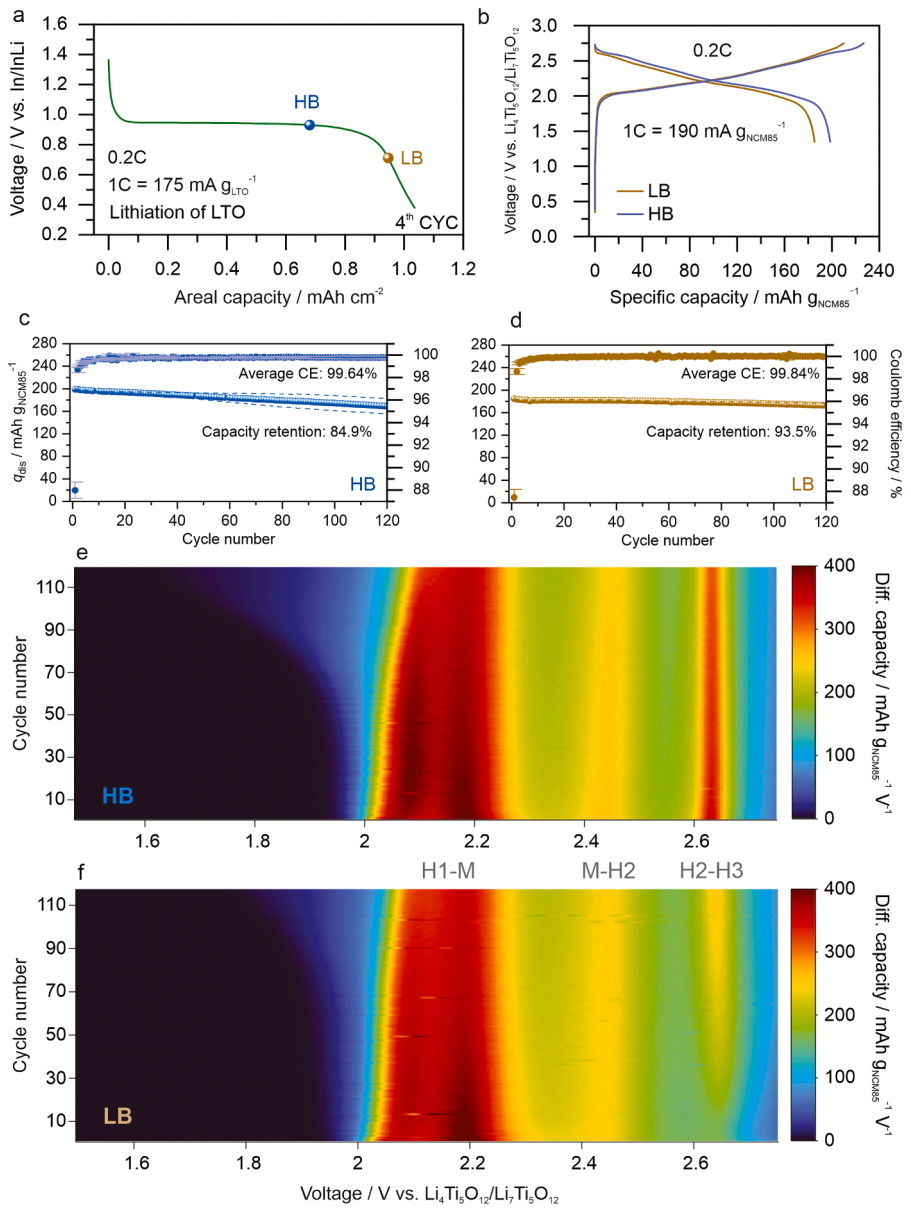

Fig. 2. Capacity balancing and electrochemical performance. (a) Fourth-cycle lithiation profile of LTO in an In/InLi|LPSCl|LTO cell at 0.2C (0.38–1.38 V vs. In/InLi). Based on Eq. 1 (see Experimental section), two n/p ratios were selected, referring to high balancing (HB, 1.5) and low balancing (LB, 1.1), as indicated by the blue and yellow dots, respectively. (b) First-cycle voltage profiles of LTO|LPSCl|$LiNbO_3$-NCM85 HB and LB cells at 0.2C (1.35–2.75 V vs. $Li_4Ti_5O_{12}/Li_7Ti_5O_{12}$). (c, d) Corresponding long-term cyclability, shown as average specific discharge capacity and Coulomb efficiency from two independent cells. The standard deviations vary from 0.9 to 13.5 mAh g^{-1}_{NCM85} and from 0.6 to 3.2 mAh g^{-1}_{NCM85} (first to 120th cycle) for the HB and LB cells, respectively. (e, f) 2D contour plots of differential capacity during charging. The characteristic phase transition ranges are specified.

representing the H1-M and M-H2 transitions overlapped well in terms of intensity and position for the HB and LB cells, while in the case of the H2-H3 peak, the intensity of the LB cells was still somewhat lower than that of the HB cells. Overall, these results confirm the effectiveness of the LB strategy in achieving stable performance of SSBs with Ni-rich cathode and sulfide SE. In the following section, the improvement in mechanical integrity is discussed in some more detail.

2.3. Cathode breathing

To find out how capacity balancing affects the mechanical stability, *operando* pressure measurements were conducted on the HB and LB cells, aiming at tracking the cathode breathing during battery operation. Given that LTO was used as CE, any pressure changes are primarily due to the mechanical response of the cathode. The respective cells were again cycled under an external pressure of 81 MPa, and a force sensor was used to monitor the pressure evolution *in situ*.

After 12 h rest at open circuit voltage (OCV), the cells reached thermodynamic equilibrium, and the corresponding pressure baseline was established for calibration of the signals recorded at 0.1C in the following five cycles. For layered Ni-rich oxide cathodes, it is well known that the lattice parameter *a* decreases upon delithiation (charge), while *c* initially increases and then drops sharply in the H2-H3 region [25–27]. This anisotropic behavior eventually results in a volume contraction that is responsible for the pressure evolution observed for the HB and LB cells (see Fig. 3a and b). As can be seen, both configurations exhibit reversible, negative net pressure changes. Interestingly, the overall pressure evolution was almost identical for the different cells over the first two cycles. This similarity could be due to initial microstructural changes within the cathode, which appear to mask the

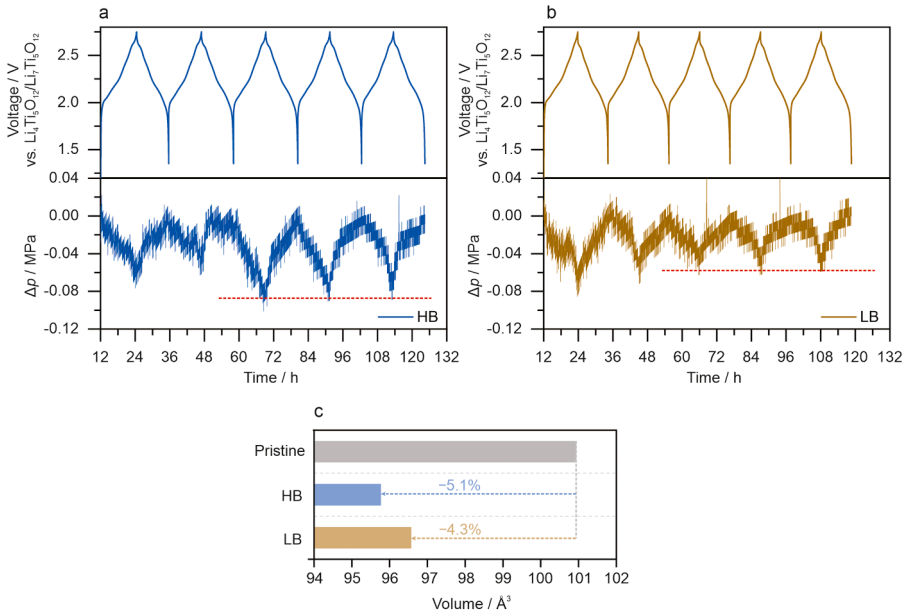

Fig. 3. Mechanical behavior of LTO|LPSCl|$LiNbO_3$-NCM85 HB and LB cells. (a, b) *Operando* pressure measurements. The cells were cycled at 0.1C (1.35–2.75 V vs. $Li_4Ti_5O_{12}/Li_7Ti_5O_{12}$) for five cycles, following a 12 h rest under OCV conditions. The corresponding voltage profiles and pressure responses are shown in the upper and lower panels, respectively. Red dotted lines indicate the extent of pressure change during cycling. (c) Unit-cell volume of $LiNbO_3$-NCM85 in the pristine state and after first charging at 0.2C. The volume contraction is indicated by dotted lines.

intrinsic volume variations of the CAM, at least to some extent.

To quantify the structural evolution of NCM85, *ex situ* XRD measurements combined with Rietveld refinement analysis were performed on harvested cathodes from the HB and LB cells after the first charge cycle and compared to their pristine state (see Figure S8). As shown in Fig. 3c and Table S2, the crystallographic volume shrinkage in the LB cells is 4.3 %, much smaller than the 5.1 % shrinkage in the HB cells. This result confirms both the successful realization of a lower UP under LB conditions and the effective suppression of lattice contraction, even during the initial formation cycles. As cycling progressed, the mechanical breathing behavior became more pronounced. From the third to fifth cycle, the LB cells exhibited a smaller negative net pressure change compared to the HB cells. This response supports the conclusion that a low n/p ratio helps improve stability, particularly within the cathode. Moreover, it correlates well with the superior capacity retention observed for the LB cells during long-term cycling, emphasizing the critical role of mitigating mechanical stresses through targeted capacity balancing.

2.4. Rate performance and post-mortem characterization

To evaluate the effects of capacity balancing on the electrochemical performance and microstructural evolution of the cathode during long-term cycling, rate capability and post-mortem analyses were performed. Specifically, the HB and LB cells were subject to sequential C-rate testing from 0.1C/0.2C to 5C for two rounds (see Fig. 4a). The corresponding specific discharge capacities are summarized in Table S3. For all C-rates, the HB cells delivered higher capacities than the LB counterpart. This is due to the lower IUP in the LB configuration, which resulted in a slightly lower specific discharge capacity from the very beginning at 0.1C (199 versus 204 mAh g_{NCM85}^{-1}). The difference in capacity was most pronounced between 0.5C and 2C, suggesting that the LB strategy with larger Ohmic polarization effectively reduces the UP across various C-rates. Nevertheless, the LB cells exhibited good rate performance. For instance, the specific discharge capacities at 1C, 2C, and 5C were found to be 164/147, 141/125, and 96/85 mAh g_{NCM85}^{-1} for HB/LB, respectively. As shown in Fig. 4f, both exhibit nearly identical normalized capacities, irrespective of the C-rate. This result shows that, despite the different n/p ratios, the use of LTO as an anode ensures consistent performance within the same cell system.

After testing the rate capability, the HB and LB cells were subject to a further 200 cycles at 0.2C (see Fig. 4b). After 90 cycles, the specific discharge capacities were similar, with q_{dis} = 191 and 189 mAh g_{NCM85}^{-1} for HB and LB, respectively. After 290 cycles, the LB cells achieved a capacity retention of ~83 %, which is higher than the ~75 % observed for the HB cells, confirming the importance of capacity balancing for long-term stability.

To determine whether there are any changes in interfacial kinetics across the cells after long-term cycling, electrochemical impedance spectroscopy (EIS) and distribution of relaxation times (DRT) analysis were performed at the end of discharge to ensure similar states of charge (SOCs) for the $LiNbO_3$-NCM85 cathode and the LTO anode (avoiding UP-induced deviations). As can be seen from the Nyquist plots (frequency domain) in Fig. 4c, both the HB and LB cells showed poorly resolved semicircles and a distinct Warburg diffusion tail at low frequencies. By converting the impedance data from frequency to time domain for DRT analysis (see Fig. 4d), six distinct peaks (P1–P6) were identified and divided into three characteristic regimes, namely, (i) high-frequency region ($\tau < 10^{-5}$ s; attributed to SE grain boundaries and particle contact), (ii) intermediate-frequency region (10^{-5} s $< \tau < 10^{-2}$ s; attributed to as-formed interphases [R_{int}], including cathode electrolyte interphase [CEI] and solid electrolyte interphase (SEI) at the anode), and (iii) medium-to-low frequency region (10^{-2} s $< \tau < 1$ s; attributed to charge-transfer processes [R_{ct}]) [28,29]. It is important to note that the inductive and diffusive parts in the impedance data were discarded during pre-processing. Considering the overall cell configuration, the resistance contribution in the R_{int} regime is largely due to the cathode, while the R_{ct} regime encompasses contributions from both cathode and anode [6,28,29]. Given the electrochemical stability of LTO against sulfide SEs and the fact that the HB and LB cells were analyzed at a similar SOC, the differences observed in the R_{ct} regime can be attributed primarily to the cathode side.

The interface-related resistance was quantitatively evaluated by fitting the individual peaks in the DRT patterns. Without assigning them to specific physical processes, the peak areas within the defined characteristic regimes (i.e., R_{int} and R_{ct}) were examined instead for

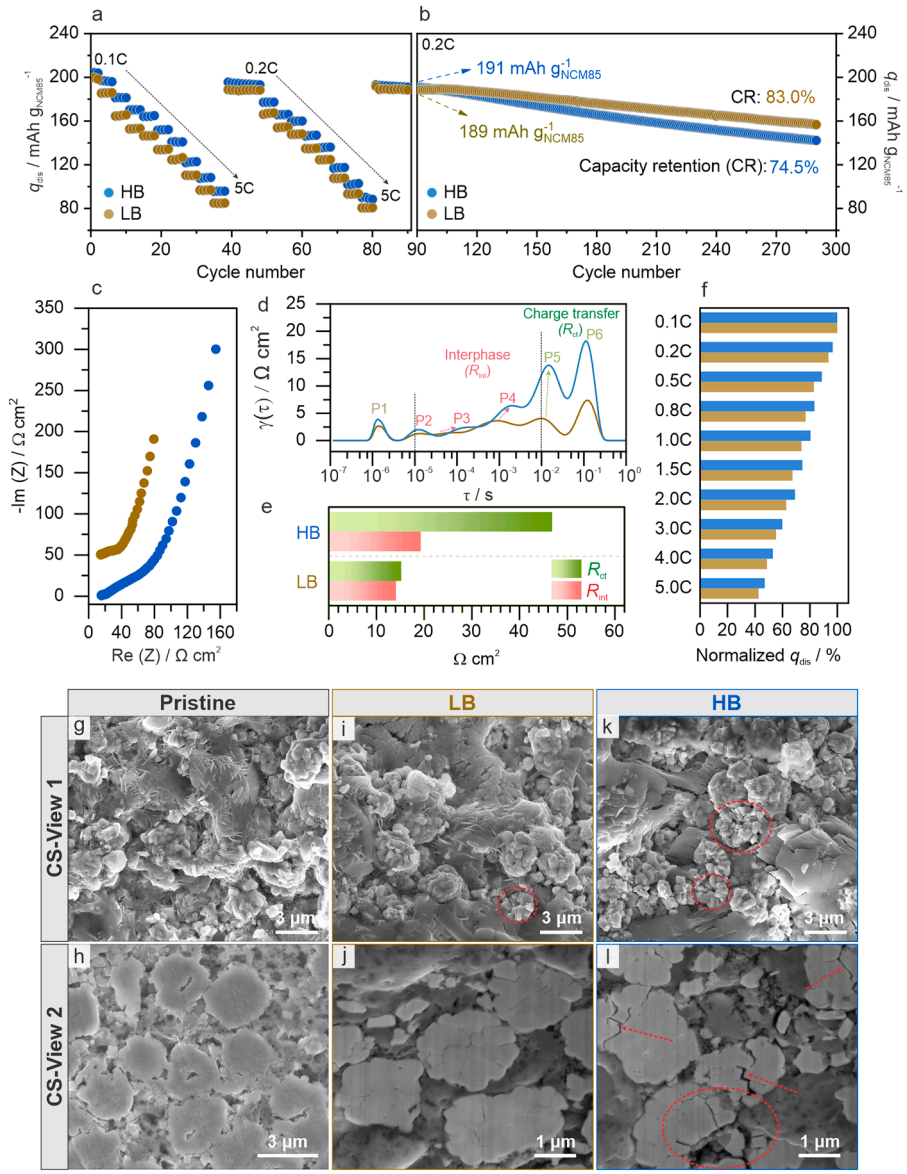

Fig. 4. Electrochemical performance of LTO|LPSCl|$LiNbO_3$-NCM85 HB and LB cells and post-mortem characterization. (a) Rate capability tested in two rounds from 0.1C/0.2C to 5C (1.35–2.75 V vs. $Li_4Ti_5O_{12}/Li_7Ti_5O_{12}$) and (b) subsequent long-term cycling at 0.2C. (c) Nyquist plots of the electrochemical impedance measured from 1 MHz to 100 mHz at the end of discharge after long-term cycling. The LB data is offset along the imaginary axis for clarity. (d) Corresponding DRT patterns with segmented kinetic time constants in the time domain for the as-formed interphases (R_{int}, with $\tau = 10^{-5}$ to 10^{-2} s) and charge-transfer processes (R_{ct}, with $\tau = 10^{-2}$ to 1 s) regimes. The inductive and diffusive parts at high and low frequencies were discarded. (e) Comparison of R_{int} and R_{ct}. (f) Normalized discharge capacities from rate-performance testing. (g–l) Cross-sectional SEM images collected from the cathode in the pristine state and after long-term cycling (discharged state). CS-View 1 and CS-View 2 refer to mechanically exposed and polished/FIB-cut areas. The dotted red circles/ellipses and arrows indicate the mechanical degradation.

determining cumulative resistance contributions, as presented in Fig. 4e and Tables S4 and S5. The results indicate that, due to the $LiNbO_3$ coating being present on the NCM85 particles, the R_{int} values are relatively low and comparable between the cells (19.3/14.1 Ω cm^2). However, there is a significant difference in the R_{ct}; it is more than three times larger for the HB cells (46.8 versus 15.2 Ω cm^2). We attribute this difference to microstructural degradation, such as particle fracture and/or void formation, which strongly impedes charge transfer. From the data, it appears that the LB cells are capable of retaining better structural integrity, thus effectively mitigating the growth of charge-transfer resistance during battery operation. This means the preserved microstructure enables more stable electrochemical behavior and contributes to the superior cycling performance observed under LB conditions.

To corroborate the above results, cross-sectional SEM analysis was performed (see Fig. 4g–l). Specifically, two types of imaging techniques were used, namely, (i) mechanical fracturing to expose the bulk cathode (CS-View 1) and (ii) focused-ion beam (FIB) cutting or Ar-ion polishing to reveal the internal structure of the CAM particles (CS-View 2). In their pristine state (see Fig. 4g and h), the $LiNbO_3$-NCM85 particles were structurally intact (i.e., showing no obvious cracking) and tightly embedded in the cathode matrix. Only a few voids in the interior were observed, which originate from the synthesis process [30]. After cycling, a clear difference between the HB and LB cathodes was noticeable. In the LB cells (see Fig. 4i and j), the structural integrity of the secondary particles remained largely intact. Although some fractured particles were observed, the grains (primary particles) remained well connected, and no signs of pulverization and/or interfacial delamination were found. Note that intimate CAM|SE contact facilitates lithium and electron transport, which is consistent with the lower R_{ct} discussed previously. In the HB cells (see Fig. 4k and l), on the other hand, severe

mechanical degradation was apparent. As expected, larger volume changes and local stress concentrations lead to mechanical failure, which ultimately results in a strongly deteriorated microstructure. The low-magnification SEM images in Figure S9 confirm this observation.

To further evaluate the longevity and performance limitations of the sulfide-based SSBs, long-term cycling tests were performed at 1C, as shown in Fig. 5. For this purpose, both the HB and LB cells with similar areal loadings of 8–9 mg_{NCM85} cm^{-2} were first subject to a short C-rate sequence at 0.1, 0.2, 0.5, 1, and 2C, followed by continuous cycling at 1C. The resulting specific discharge capacities for the HB (203, 195, 178, 160, and 134 mAh g_{NCM85}^{-1}) and LB cells (201, 189, 167, 148, and 124 mAh g_{NCM85}^{-1}) were consistent with the above results (see Fig. 4a and Table S3), confirming the reproducibility of the electrochemical behavior. During the subsequent cycling at 1C, the HB and LB cells initially delivered specific discharge capacities of q_{dis} = 161 and 149 mAh g_{NCM85}^{-1}, respectively. However, with prolonged cycling, a noticeable difference in stability became apparent. The HB cells maintained 80 % of their initial capacity after 414 cycles and delivered 111 mAh g_{NCM85}^{-1} after 718 cycles, corresponding to a capacity retention of ~69 %. In contrast, the LB cells achieved around 80 % capacity retention over 1318 cycles, which corresponds to a 3.2-fold increase in cycle life, and still retained 111 mAh g_{NCM85}^{-1} after 1575 cycles (equivalent to 75 % retention). This improvement is solely attributable to the LB strategy. Notably, both cells exhibited high Coulomb efficiencies throughout cycling, averaging 99.9 % for HB and 100 % for LB.

In summary, the LB condition leads to increased cathode stability, which is associated with improved capacity retention. The lower IUP mitigates (early-stage) lattice contraction and stress-induced cracking of the $LiNbO_3$-NCM85 secondary particles. Over the course of cycling, polarization—due to electro-chemo-mechanical effects—leads to an increase in UP, which in turn provides additional capacity to compensate for losses caused by adverse side reactions and degradation. The gradually increasing volume changes apparently create more spatial and temporal tolerance for the adaptation of the electrode components to each other, thereby increasing the effectiveness of the LB strategy in terms of enhancing electrochemical and mechanical robustness in SSB systems.

2.5. Mechanistic considerations

To verify the functionality of the tip-shaped lithiation tail of LTO under LB conditions and for various C-rates, a three-electrode (3E) analysis is essential. The strategy is based on exploiting the region near the end of lithiation to enable a lower IUP instead of the DUP. However, this subtle deviation from the voltage plateau cannot be captured in conventional two-electrode (2E) cell setups. Instead, 3E measurements are required to deconvolute the contributions of individual electrodes to the voltage profile and determine whether the proposed mechanism actually occurs. We have therefore developed an advanced 3E setup for SSBs using prelithiated LTO as the RE, which provides a stable and well-defined reference potential of 1.55 V vs. Li^+/Li. Details on the cell design are provided in the Experimental section and in previous work [29].

As shown in Figure S10, a rate capability test from 0.2C to 5C was conducted on the 3E LB cells using a protocol similar to that of the 2E cells (see Fig. 4a). In fact, their electrochemical performance showed strong consistency with the 2E counterpart across all C-rates, as summarized in Table S6, confirming the accuracy and robustness of the measurement setup. The deconvoluted potential profiles of the $LiNbO_3$-NCM85 WE and LTO CE are presented in Fig. 6a. As highlighted by the green dotted circles, the LTO potential did indeed show a distinct tip-shaped behavior toward the end of charging, even after several cycles at different C-rates. This confirms that the lithiation tail persists and remains active in the compensation mechanism. In parallel, by examining the end-of-charge potential of the $LiNbO_3$-NCM85 WE (see red dotted circles), a gradual increase in UP throughout cycling was observed, from 4.1919 V vs. Li^+/Li in the initial cycle to 4.1931 V in the second cycle, and up to 4.2237 V after returning back to 0.2C in the 24th cycle. This trend strongly supports our hypothesis that polarization causes a gradual increase in UP, enabling capacity compensation during SSB operation. Of note, with respect to the corresponding lower cut-off potential of the LTO CE, the cell voltage calculated from the WE/CE remained essentially unaltered (relative to the pre-defined window of 1.35 to 2.75 V vs. $Li_4Ti_5O_{12}/Li_7Ti_5O_{12}$). A summary of the cut-off potentials of WE and CE, together with the resulting cell voltage at the end of charge and discharge during rate performance testing of the LB cells, is provided in Table S7. Individual potential profiles for selected C-rates are presented in Fig. 6b–e. As is evident, the tip-shaped lithiation tail of LTO was consistently observed across all C-rates, further validating the robustness of the proposed LB strategy and making the approach highly relevant for practical SSB applications.

In general, the performance of Ni-rich cathodes paired with sulfide SEs strongly depends on the mechanical stability given that detrimental side reactions are effectively suppressed by interface engineering. Therefore, the key to balancing between capacity and stability lies in regulating the mechanical behavior of the electrode active materials, particularly the CAM. The excellent long-term performance achieved here is based on an adaptive compensation process that is maintained throughout cycling. To provide a better understanding of this mechanism under different capacity balancing conditions, Fig. 7 shows schematic representations summarizing the principles underlying it.

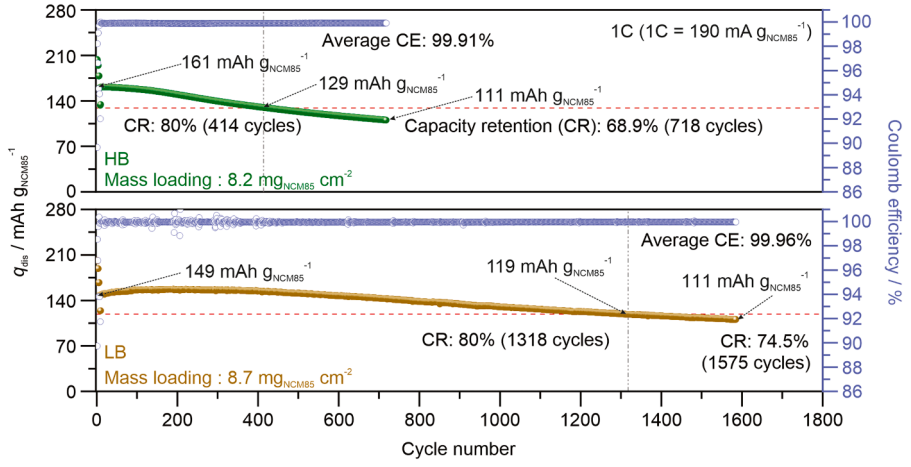

Fig. 5. Long-term cycling performance of LTO|LPSCl|$LiNbO_3$-NCM85 HB and LB cells at 1C (1.35–2.75 V vs. $Li_4Ti_5O_{12}/Li_7Ti_5O_{12}$). At the beginning, a C-rate test from 0.1C to 2C was performed.

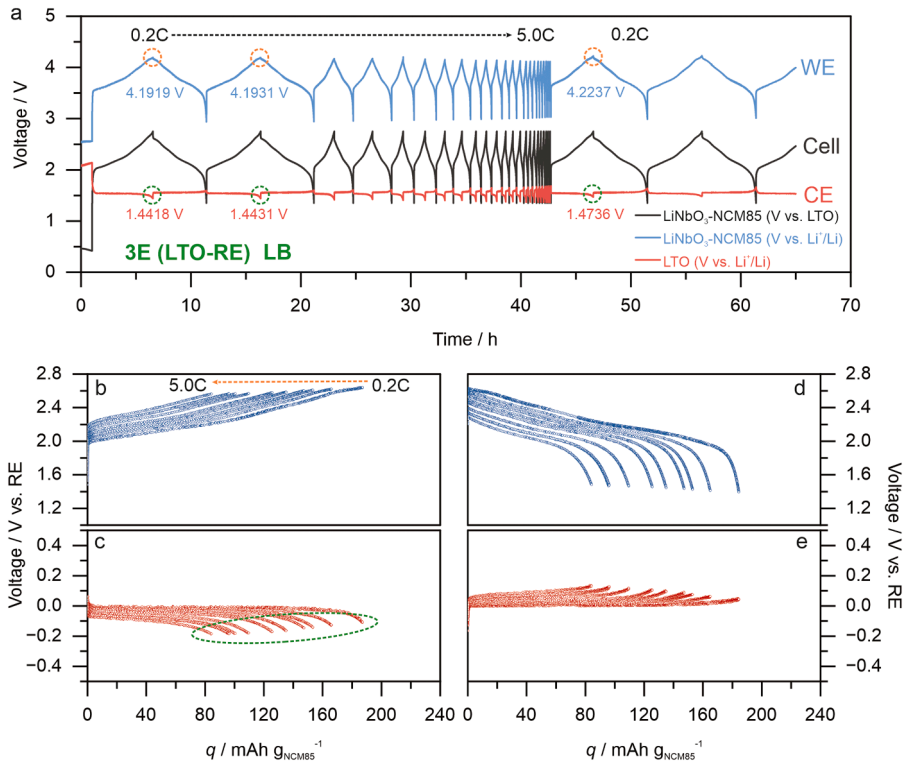

Fig. 6. Three-electrode analysis of an LB cell during rate capability testing from 0.2C to 5C. (a) Deconvoluted potential profiles of the $LiNbO_3$-NCM85 WE and LTO CE and cell voltage (WE/CE) shown in blue, red, and black, respectively. The potential of the WE and CE is referenced to Li^+/Li using an LTO reference electrode (LTO-RE, 1.55 V vs. Li^+/Li). The red and green dotted circles indicate the behavior upon approaching end of charge/discharge of the $LiNbO_3$-NCM85/LTO. Selected potential profiles (b) of the NCM85 WE (delithiation) and (c) LTO CE (lithiation) at various C-rates referenced to the LTO-RE. The green dotted ellipse indicates the deviation of the LTO potential from its plateau near the end of the charging process. Corresponding potential profiles (d) of the NCM85 WE (lithiation) and (e) LTO CE (delithiation).

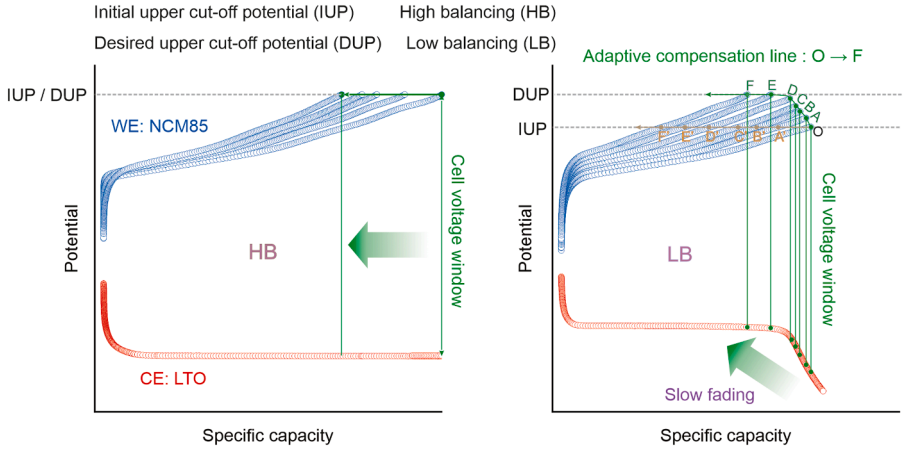

Fig. 7. Schematic representation of the proposed adaptive compensation through capacity balancing. For HB cells, the IUP of the WE corresponds to the DUP. For LB cells, there is a discrepancy between IUP and DUP, which is limited by the pre-defined voltage window. Upon cycling, due to capacity loss caused by polarization, the UP increases along the compensation line from O to F. With the HB design, faster capacity degradation is observed along the line from O to F'.

Under HB conditions, the LTO CE was found to operate entirely within the 1.55 V plateau, enabling the NCM85 WE to reach the DUP of 4.3 V vs. Li^+/Li in each cycle [31]. However, electro-chemo-mechanical degradation inevitably occurs, causing increasing polarization, which ultimately leads to capacity fading and poor stability. In the HB case, the system clearly lacks flexibility, as the IUP and DUP are the same, meaning that it cannot respond to changes in polarization unless the voltage window is adjusted manually. Consequently, there is no intrinsic mechanism that can compensate for capacity decay.

Under LB conditions, the cathode initially terminates the delithiation at a lower upper cut-off potential of ~4.2 V vs. Li^+/Li. This is due to the tip-shaped lithiation tail of LTO, with the CE deviating from the 1.55 V plateau as the cell approaches the charge cut-off. Overall, the LB configuration offers two distinct advantages: (i) it somewhat lowers the (initial) degree of cathode delithiation, thereby mitigating mechanical degradation by alleviating the H2-H3 phase transition and also reducing side reactions at the CAM|SE interface, and (ii) it creates a discrepancy between IUP and DUP, resulting in a kind of capacity reservoir/buffer that is gradually exploited to compensate for polarization-related capacity losses and thus extends longevity. The decoupling of IUP and DUP

distinguishes LB from HB, where such compensation is not possible. During cycling, the cathode's UP increases gradually and eventually approaches the DUP, as indicated by the compensation line (from O to F) in Fig. 7. The latter not only ensures dynamic capacity recovery, but also prevents severe volume changes. Apparently, this self-regulated voltage evolution gives the cathode sufficient time to adapt structurally and electrochemically, which in turn positively affects stability and cyclability. However, it does not completely prevent mechanical degradation, as the effect eventually reaches its limits when the LTO potential returns to the plateau region. Nevertheless, the LB strategy offers an effective means of delaying the onset of instability.

3. Conclusions

In this work, which aimed to develop high-performance SSBs with Ni-rich cathode and thiophosphate SE, we propose a capacity balancing strategy using LTO as anode for achieving an optimal compromise between capacity (energy density) and stability. Under low balancing conditions, the effective initial upper cut-off potential of the cathode was found to be lower than the targeted one, resulting in a partially suppressed H2-H3 phase transition, thereby reducing the net volume change of the active material during (de)lithiation and mitigating the mechanical stresses that normally lead to particle fracture and/or interfacial delamination. Over the course of electrochemical cycling, the polarization caused by electro-chemo-mechanical degradation gradually increased the cut-off potential, as also confirmed by 3E measurements, ultimately enabling adaptive compensation for capacity loss. This mechanism significantly extended the longevity without requiring active control of the voltage window. In fact, the low balancing cells had a cycle life (80 % capacity retention) at 1C rate more than three times longer than that of the high balancing cells.

Taken together, this study demonstrates that capacity balancing is a simple, yet powerful approach to improving the stability of Ni-rich cathodes in sulfide SSBs. LTO served not only as a model electrode, but can also be considered a conceptual bridge for the development/use of newly developed alloy-type (energy-dense) anodes that are compatible with adaptive compensation schemes.

4. Experimental section

All preparation steps, including those for the materials, composites, electrodes, and cell assembly, were performed in Ar environments, involving among others sealed ball-milling jars and gloveboxes with $p(H_2O)/p < 0.1$ ppm and $p(O_2)/p < 0.1$ ppm.

4.1. $LiNbO_3$ coating

Prior to coating, polycrystalline NCM85 ($d_{50} \approx 4$ μm, BASF SE) was heated at 750 °C for 3 h under an O_2 atmosphere to remove surface impurities. The procedure for $LiNbO_3$ sol-gel-type coating followed our previous work [13]. To achieve a nominal coating content of 1 wt. %, 410 μL lithium (1.0 M) and 820 μL niobium ethoxide solutions (0.5 M) were added to 5.94 g of NCM85, along with 1 mL of absolute ethanol. The resulting mixture was ultrasonicated for 15 min and subsequently dried under vacuum. The obtained powder was then calcined at 350 °C for 2 h under an O_2 atmosphere, yielding $LiNbO_3$-NCM85.

4.2. Preparation of cathode and anode composites

Li_6PS_5Cl (LPSCl, NEI Corp.) and Super C65 (TIMCAL Ltd.) were used as SE and conductive carbon additive, respectively. The weight ratios of the components were 69.3:29.7:1.0 for $LiNbO_3$-NCM85:LPSCl:Super C65 (cathode composite) and 30:65:5 for LTO:LPSCl:Super C65 (anode composite). For 1 g of composite, 10 ZrO_2 balls (10 mm in diameter) were added, and the mixture was ball-milled at 140 rpm for 30 min using an 80 mL jar.

4.3. Preparation of slurry-cast cathodes

The as-prepared composite was used to fabricate slurry-cast cathode tapes. Anhydrous *o*-xylene (97 %, Sigma-Aldrich) and polyisobutylene (Oppanol N150, BASF SE) served as solvent and polymer binder, respectively. The cathode composite was first pre-wetted and subsequently mixed with 1 wt. % binder. The weight ratio of the components was 68.6:29.4:1.0:1.0 for $LiNbO_3$-NCM85:LPSCl:Super C65:Oppanol N150. After thorough mixing, the slurry was cast onto Al foil, followed by drying. Circular electrodes with a diameter of 9 mm were punched out for electrochemical measurements. Further details of the procedure can be found elsewhere [19,22].

4.4. Capacity balancing

In this work, the balancing between the $LiNbO_3$-NCM85 cathode and the LTO anode was realized by adjusting the mass of the LTO composite. Specifically, the capacities achieved in the fourth cycle at 0.2C rate (after cell formation) were used as initial values in the calculations, namely, a specific charge (delithiation) capacity of 202 mAh g^{-1} for $LiNbO_3$-NCM85 and a specific discharge (lithiation) capacity of 132 mAh g^{-1} for LTO, as shown in Figure S4. The balancing factor B was defined, and the mass of $LiNbO_3$-NCM85 (m_{CAM}, in grams) was used to determine the corresponding LTO mass (m_{LTO}) via the following equation:

$$m_{LTO} = B \cdot m_{CAM} \cdot \frac{202\ \text{mAh g}^{-1}}{132\ \text{mAh g}^{-1}}. \quad (1)$$

The required mass of LTO composite was then calculated based on the ratio of components mentioned above.

4.5. SSB assembly

In-house designed setups for two-electrode (2E) and three-electrode (3E) cells were used for SSB testing. Each cell consisted of a PEEK ring (10 mm in diameter; for 3E, two symmetrical holes were drilled) and two stainless steel current collectors. For 2E cells, 100 mg of SE was first pre-pressed at 63 MPa to form the separator layer. The punched cathode tape, with CAM loadings of 8–9 mg cm^{-2}, was placed on one side of the separator layer, while a certain amount of LTO composite (based on the balancing strategy) was added to the opposite side. The cells were then pressed at 435 MPa for 3 min. For cells with an In/InLi counter electrode (CE), the working electrode (WE), either the cathode tape or the LTO composite, was placed onto the separator layer, followed by pressing at 435 MPa for 3 min. Indium (9 mm in diameter, 100 μm thick, Changsha Santech Materials Co., Ltd.) and lithium foil discs (6 mm in diameter, 50 μm thick, Albemarle Germany GmbH) were stacked in sequence on the opposite side. For 3E cells, the preparation of the reference electrode (RE) and the assembly procedure followed previous work [29]. The LTO composite was used as LTO-RE, with a stainless steel wire (0.127 mm in diameter, Thermo Fisher Scientific) serving as current collector. The LTO-RE was embedded in the center of a thickened separator layer (160 mg). The subsequent assembly of WE and CE followed the same procedure as that for the 2E cells.

4.6. Galvanostatic cycling

The SSB cells were cycled using a MACCOR battery cycler. When $LiNbO_3$-NCM85 served as cathode (WE), the potential was set between 2.9 and 4.3 V vs. Li^+/Li. Depending on the choice of CE, the cell voltage was adjusted accordingly: with LTO (1.55 V vs. Li^+/Li), the window was set to 1.35–2.75 V vs. $Li_4Ti_5O_{12}/Li_7Ti_5O_{12}$, and with In/InLi (0.62 V vs. Li^+/Li), it was set to 2.28–3.68 V vs. In/InLi. When LTO was used as WE, the potential range was approx. 1.0–2.0 V vs. Li^+/Li, corresponding to 0.38–1.38 V vs. In/InLi. The current was defined based on the specific C-

rate, with 1C = 190 mA g^{-1}_{NCM85} for $LiNbO_3$-NCM85 and 1C = 175 mA g^{-1}_{LTO} for LTO. 3E cells were sealed in a pouch bag and cycled at 45 °C and under an external pressure of 81 MPa based on the voltage between WE and CE.

4.7. Powder X-ray diffraction (XRD)

CAM (pristine NCM85 or $LiNbO_3$-NCM85) was loaded into 0.3 mm borosilicate capillaries (Hilgenberg), while 0.5 mm capillaries were used for the cathode composite. Diffraction data was collected in Debye–Scherrer geometry using a STOE Stadi-P diffractometer equipped with a Mo anode (λ = 0.7093 Å) and a DECTRIS MYTHEN 1 K strip detector. LaB_6 standard reference material was used to evaluate the instrumental peak broadening. GSAS-II software was used for Rietveld refinement [32]. For determining the crystallographic parameters of NCM85, the scale factor, zero shift, and size/strain broadening parameters were refined. A fixed background function using a 13-term Chebyshev polynomial was applied. The lattice parameters, oxygen *z*-coordinate, and atomic displacement parameters for each site were refined. Atoms occupying the same site were constrained to have the same atomic parameters, and site occupancy factors were constrained such that each site remained fully occupied.

4.8. Scanning electron microscopy coupled with energy-dispersive X-ray spectroscopy (SEM-EDS)

Morphological and elemental analyses were performed using a Leo 1530 microscope (Zeiss) equipped with a field-emission gun. For elemental mapping via EDS, an Oxford X-Max^N detector (Oxford Instruments) was used.

4.9. Cross-sectional imaging

The pristine cathode tape was polished by Ar-ion milling using an IB19510CP cross-section polisher (JEOL). Cycled samples were sectioned using a dual-beam focused ion beam (FIB) system (FEI Strata 400) with Ga^+ ion source operated at 30 kV. To minimize potential impact from air exposure during characterization, the samples were mounted onto a stage within an Ar-filled glovebox and immediately transferred to the FIB chamber using a sealed packaging bag. Throughout this process, the samples were exposed to air for less than 20 s.

4.10. Electrochemical impedance spectroscopy coupled with distribution of relaxation times analysis (EIS-DRT)

Potentiostatic EIS (PEIS) measurements were performed using a Bio-Logic SP-300 multichannel potentiostat. The cells were rested for 1 h at the end of either charge or discharge prior to the impedance measurements. Spectra were recorded over a frequency range from 1 MHz to 100 mHz, with a perturbation amplitude of 10 mV. DRT analysis was performed by processing the complex impedance data after subtracting the inductive (high-frequency) and capacitive (low-frequency) contributions. A Gaussian radial basis function (RBF)-based discretization method was applied, using a shape factor of 0.5 and a regularization parameter of $\lambda = 10^{-4}$ for all spectra. Multiple Gaussian functions were used to fit the peaks in the DRT patterns, enabling quantitative analysis of interfacial kinetics within the relaxation time constant between 10^{-5} and 1 s [29].

4.11. Operando pressure measurements

A force sensor (KM26 10 kN, ME-Meßsysteme GmbH) was mounted on top of a sealed cell and clamped in a rigid frame, applying an initial load of 6.35 kN (equivalent to 81 MPa). The dynamic force, due to volume changes of the $LiNbO_3$-NCM85 cathode during cycling, was recorded continuously. An initial 12 h resting period at 45 °C allowed for mechanical relaxation, and the stabilized force value served as baseline for the subsequent galvanostatic measurements. The cells were cycled for five cycles at 0.1C rate within the voltage window defined for the $LiNbO_3$-NCM85 cathode and LTO anode using a Bio-Logic VMP-3 multichannel potentiostat.

CRediT authorship contribution statement

Ruizhuo Zhang: Writing – original draft, Visualization, Validation, Methodology, Investigation, Formal analysis, Data curation, Conceptualization. **Seyedhosein Payandeh:** Writing – review & editing, Validation, Conceptualization. **Yuan Ma:** Writing – review & editing. **Damian Goonetilleke:** Writing – review & editing, Validation, Formal analysis. **Yushu Tang:** Writing – review & editing, Validation, Investigation, Formal analysis. **Aleksandr Kondrakov:** Writing – review & editing, Supervision, Project administration, Funding acquisition. **Jürgen Janek:** Writing – review & editing, Supervision. **Torsten Brezesinski:** Writing – review & editing, Supervision, Project administration, Funding acquisition.

Declaration of competing interest

The authors declare that they have no known competing financial interests or personal relationships that could have appeared to influence the work reported in this paper.

Acknowledgements

This study was supported by BASF SE. The authors acknowledge the support from the Karlsruhe Nano Micro Facility (KNMFi, www.knmf.kit.edu), a Helmholtz research infrastructure at Karlsruhe Institute of Technology (KIT, www.kit.edu).

Supplementary materials

Supplementary material associated with this article can be found, in the online version, at doi:10.1016/j.ensm.2026.105045.

Data availability

Data will be made available on request.

References

[1] J. Janek, W.G. Zeier, Challenges in speeding up solid-state battery development, Nat. Energy 8 (2023) 230.
[2] J. Janek, W.G. Zeier, A solid future for battery development, Nat. Energy 1 (2016) 16141.
[3] C. Wang, J. Liang, Y. Zhao, M. Zheng, X. Li, X. Sun, All-solid-state lithium batteries enabled by sulfide electrolytes: from fundamental research to practical engineering design, Energy Environ. Sci. 14 (2021) 2577–2619.
[4] D. Ren, L. Lu, R. Hua, G. Zhu, X. Liu, Y. Mao, X. Rui, S. Wang, B. Zhao, H. Cui, M. Yang, H. Shen, C.-Z. Zhao, L. Wang, X. He, S. Liu, Y. Hou, T. Tan, P. Wang, Y. Nitta, M. Ouyang, Challenges and opportunities of practical sulfide-based all-solid-state batteries, eTransportation 18 (2023) 100272.
[5] Y. Kato, S. Hori, T. Saito, K. Suzuki, M. Hirayama, A. Mitsui, M. Yonemura, H. Iba, R. Kanno, High-power all-solid-state batteries using sulfide superionic conductors, Nat. Energy 1 (2016) 16030.
[6] W. Zhao, R. Zhang, F. Ren, L. Karger, S.L. Dreyer, J. Lin, Y. Ma, Y. Cheng, A.S. Pal, M. Velazquez-Rizo, A. Ahmadian, Z. Zhang, P. Muller, J. Janek, Y. Yang, A. Kondrakov, T. Brezesinski, Protective coating of single-crystalline Ni-rich cathode enables fast charging in all-solid-state batteries, ACS Nano 19 (2025) 8595–8607.
[7] M.K. Jangid, T.H. Cho, T. Ma, D.W. Liao, H. Kim, Y. Kim, M. Chi, N.P. Dasgupta, Eliminating chemo-mechanical degradation of lithium solid-state battery cathodes during >4.5 V cycling using amorphous Nb_2O_5 coatings, Nat. Commun. 15 (2024) 10233.
[8] Y.-G. Lee, S. Fujiki, C. Jung, N. Suzuki, N. Yashiro, R. Omoda, D.-S. Ko, T. Shiratsuchi, T. Sugimoto, S. Ryu, J.H. Ku, T. Watanabe, Y. Park, Y. Aihara, D. Im, I.T. Han, High-energy long-cycling all-solid-state lithium metal batteries enabled by silver–carbon composite anodes, Nat. Energy 5 (2020) 299–308.

[9] A. Banerjee, X. Wang, C. Fang, E.A. Wu, Y.S. Meng, Interfaces and interphases in all-solid-state batteries with inorganic solid electrolytes, Chem. Rev. 120 (2020) 6878–6933.
[10] R. Zhang, F. Strauss, L. Jiang, L. Casalena, L. Li, J. Janek, A. Kondrakov, T. Brezesinski, Transition-metal interdiffusion and solid electrolyte poisoning in all-solid-state batteries revealed by cryo-TEM, Chem. Commun. 59 (2023) 4600–4603.
[11] W.D. Richards, L.J. Miara, Y. Wang, J.C. Kim, G. Ceder, Interface stability in solid-state batteries, Chem. Mater. 28 (2015) 266–273.
[12] S. Payandeh, C. Njel, A. Mazilkin, J.H. Teo, Y. Ma, R. Zhang, A. Kondrakov, M. Bianchini, T. Brezesinski, The effect of single versus polycrystalline cathode particles on all-solid-state battery performance, Adv. Mater. Interfaces 10 (2022) 2201806.
[13] A.Y. Kim, F. Strauss, T. Bartsch, J.H. Teo, T. Hatsukade, A. Mazilkin, J. Janek, P. Hartmann, T. Brezesinski, Stabilizing effect of a hybrid surface coating on a Ni-rich NCM cathode material in all-solid-state batteries, Chem. Mater. 31 (2019) 9664–9672.
[14] R.N. Wullich, B. Lelotte, V. Pelé, C. Jordy, L. Gubler, M. El Kazzi, Optimized $LiNbO_3$ sol-gel coatings for NCM622 in sulfide-based all-solid-state batteries: insights into synthesis, uniformity, and electrochemical performance, Electrochim. Acta 536 (2025) 146750.
[15] L.R. Mangani, C. Villevieille, Mechanical vs. chemical stability of sulphide-based solid-state batteries. Which one is the biggest challenge to tackle? Overview of solid-state batteries and hybrid solid state batteries, J. Mater. Chem. A 8 (2020) 10150–10167.
[16] S. Kalnaus, N.J. Dudney, A.S. Westover, E. Herbert, S. Hackney, Solid-state batteries: the critical role of mechanics, Science 381 (2023) eabg5998.
[17] J.A. Lewis, J. Tippens, F.J.Q. Cortes, M.T. McDowell, Chemo-mechanical challenges in solid-state batteries, Trends Chem 1 (2019) 845–857.
[18] J.H. Teo, F. Strauss, F. Walther, Y. Ma, S. Payandeh, T. Scherer, M. Bianchini, J. Janek, T. Brezesinski, The interplay between (electro)chemical and (chemo) mechanical effects in the cycling performance of thiophosphate-based solid-state batteries, Mater. Futures 1 (2022) 015102.
[19] Y. Ma, R. Zhang, Y. Tang, Y. Ma, J.H. Teo, T. Diemant, D. Goonetilleke, J. Janek, M. Bianchini, A. Kondrakov, T. Brezesinski, Single- to few-layer nanoparticle cathode coating for thiophosphate-based all-solid-state batteries, ACS Nano 16 (2022) 18682–18694.
[20] Y. Ma, R. Zhang, Y. Ma, T. Diemant, Y. Tang, S. Payandeh, D. Goonetilleke, D. Kitsche, X. Liu, J. Lin, A. Kondrakov, T. Brezesinski, Interface and electrode microstructure engineering for optimizing performance of the $LiNiO_2$ cathode in all-solid-state batteries, Chem. Mater. 36 (2024) 2588–2598.
[21] C. Mao, J. Dong, J. Li, X. Zhai, J. Ma, S. Luan, X. Shen, Y. Wang, P. Zhang, H. Sun, X. Bie, X. Gao, J. Song, Toward practical all-solid-state batteries: current status of functional binders, Adv. Mater. 37 (2025) e2500079.
[22] J.H. Teo, F. Strauss, Đ. Tripković, S. Schweidler, Y. Ma, M. Bianchini, J. Janek, T. Brezesinski, Design-of-experiments-guided optimization of slurry-cast cathodes for solid-state batteries, Cell Rep. Phys. Sci. 2 (2021) 100465.
[23] Y. Lu, C.-Z. Zhao, H. Yuan, J.-K. Hu, J.-Q. Huang, Q. Zhang, Dry electrode technology, the rising star in solid-state battery industrialization, Matter 5 (2022) 876–898.
[24] S. Puls, E. Nazmutdinova, F. Kalyk, H.M. Woolley, J.F. Thomsen, Z. Cheng, A. Fauchier-Magnan, A. Gautam, M. Gockeln, S.Y. Ham, M.T. Hasan, M.G. Jeong, D. Hiraoka, J.S. Kim, T. Kutsch, B. Lelotte, P. Minnmann, V. Miss, K. Motohashi, D. L. Nelson, F. Ooms, F. Piccolo, C. Plank, M. Rosner, S.E. Sandoval, E. Schlautmann, R. Schuster, D. Spencer-Jolly, Y.P. Sun, B.S. Vishnugopi, R.Z. Zhang, H. Zheng, P. Adelhelm, T. Brezesinski, P.G. Bruce, M. Danzer, M. El Kazzi, H. Gasteiger, K. B. Hatzell, A. Hayashi, F. Hippauf, J. Janek, Y.S. Jung, M.T. McDowell, Y.S. Meng, P.P. Mukherjee, S. Ohno, B. Roling, A. Sakuda, J. Schwenzel, X.L. Sun, C. Villevieille, M. Wagemaker, W.G. Zeier, N.M. Vargas-Barbosa, Benchmarking the reproducibility of all-solid-state battery cell performance, Nat. Energy 9 (2024) 1310–1320.
[25] Y. Huang, P. Li, H. Wei, Y.H. Luo, M. Chen, S. Liu, W. Yin, X.H. Zhang, J.C. Zheng, Revealing the correlation between structural evolution and reversible phase transition of single-crystalline Ni-rich cathode, ACS Nano 19 (2025) 23719–23731.
[26] D. Goonetilleke, N. Sharma, W.K. Pang, V.K. Peterson, R. Petibon, J. Li, J.R. Dahn, Structural evolution and high-voltage structural stability of $Li(Ni_xMn_yCo_z)O_2$ electrodes, Chem. Mater. 31 (2018) 376–386.
[27] D. Goonetilleke, F. Riewald, A.O. Kondrakov, J. Janek, T. Brezesinski, M. Bianchini, Alleviating anisotropic volume variation at comparable Li utilization during cycling of Ni-rich, Co-free layered oxide cathode materials, J. Phys. Chem. C 126 (2022) 16952–16964.
[28] Y. Lu, C.-Z. Zhao, J.-Q. Huang, Q. Zhang, The timescale identification decoupling complicated kinetic processes in lithium batteries, Joule 6 (2022) 1172–1198.
[29] R. Zhang, A. Kondrakov, J. Janek, T. Brezesinski, Timescale identification of electrochemical processes in all-solid-state batteries using an advanced three-electrode cell setup, Energy Storage Mater. 75 (2025) 104000.
[30] J. Wang, B. Batara, K. Xu, K. Zhang, W. Hua, Y. Peng, W. Liu, A.H.I. Putri, Y. Xu, X. Sun, X. Li, Co-precipitation of Ni-rich $me(OH)_2$ precursors for high performance $LiNi_xMn_yCo_{1-x-y}O_2$ cathodes: A review, Energy Environ. Mater. 8 (2025) e70078.
[31] R. Zhang, A. Kondrakov, J. Janek, T. Brezesinski, Interfacial anode kinetics and its influence on cycling performance of sulfide solid-state batteries, ACS Nano 20 (2026) 1225–1237.
[32] B.H. Toby, R.B. Von Dreele, GSAS-II: the genesis of a modern open-source all purpose crystallography software package, J. Appl. Crystallogr. 46 (2013) 544–549.